AUTOMOTIVE LITHIUM BATTERY FAULT DIAGNOSIS COMBINING IMPROVED LSTM AND WAVELET PACKET NOISE REDUCTION ALGORITHM

Daiqiao Guo
School of Intelligent Manufacturing, Hebi Polytechnic, Hebi, 458030, China

Abstract - The number of electric vehicles has increased dramatically in recent years, and lithium battery defect detection has grown in significance. Aiming at the low accuracy of current automotive lithium battery fault diagnosis methods, this study proposes a lithium battery fault diagnosis method based on long short-term memory and wavelet packet denoising. Moreover, this study introduces an improved gray wolf optimizer that combines adaptive strategies and chaotic search algorithms to optimize long short-term memory, and constructs an improved gray wolf optimization-long short-term memory algorithm for automotive lithium battery fault diagnosis. The results found that the accuracy of the algorithm was 98.16%, and the F1 score was 97.69%. Subsequently, the application effect of the automotive lithium battery fault diagnosis model based on the improved algorithm was analyzed. According to the findings, this fault diagnosis model outperformed the comparative fault diagnosis model with diagnostic accuracy of 97.9%, 98.2%, 97.8%, and 97.4% for each of the four fault categories. In conclusion, the automobile lithium battery fault detection model put forward in this work is efficient, performs very well, and can serve as a theoretical foundation for battery fault-related research areas. Nevertheless, this study is limited by the simplified operating conditions considered, as real-world battery systems involve more complex factors affecting fault occurrence. Future work should incorporate more comprehensive influencing factors to improve practical applicability.

Keywords: Electric vehicles; Lithium batteries; Fault diagnosis; Long short-term memory network; Gray wolf optimizer; Wavelet noise reduction method.

1. Introduction

In the context of globalization of the greenhouse effect, using clean energy to replace traditional fossil energy to achieve energy conservation and emission reduction is one of the important ways to build a green society. As one of the main sources of greenhouse gas emissions, automobile emissions reduction is particularly important [1-2]. Therefore, cars powered by lithium batteries (LBs) emerged. Since cars operate under complex road conditions and environments for a long time, LBs often malfunction, and their fault diagnosis (FD) has attracted much attention. However, current LB FD methods still have low accuracy. Many scholars have done relevant research. For example, Zhao J et al. reviewed the diagnostic methods of LB faults through a literature review. It was found that combining sensors, physics, and multi-scale methods could achieve comprehensive multi-domain FD, but no specific diagnosis method was given [3].

Aiming at the problem that traditional FD methods could not detect minor battery faults in the early stage, Gu X et al. proposed a battery early FD method based on improved principal components analysis (PCA). The experimental outcomes revealed that this method had a good identification effect, but it did not involve the classification and identification of fault types [4].

To solve the problem of low accuracy of automobile LB FD, Huang J C et al. proposed a new method for fault detection of electric vehicle LB packs by using the battery's charging state and self-encoding depth. Experimental results showed that the recognition accuracy of this method was 93.18%, but the calculation was time-consuming [5]. To solve the problem of low FD accuracy of automotive LB modules, Mao Z et al. proposed a small short-circuit FD method based on extreme sample entropy. The outcomes revealed that this method could detect 100 battery cells in just 1 second, but the accuracy improvement was not ideal [6]. Liao L et al. developed a diagnostic technique based on the Laida criterion

dx.doi.org/10.17683/ijomam/issue25/v2.17

and wavelet packet (WP) decomposition to address the issue of low diagnostic accuracy (DA) of unexpected failures in automotive LBs. According to experimental findings, this approach outperformed the conventional approach, however it was not very good at identifying fault kinds [7]. Regarding the low accuracy rate of LB FD for electric vehicles, Huang J C et al. proposed a diagnostic model based on Transformer. The experimental results showed that the recognition accuracy and recall rate of this model were 93.18% and 93.37% respectively, but the computational complexity was relatively high [8]. Zhang C et al. aimed to solve the problem of low accuracy of LB fault prediction in electric vehicles, and proposed a FD method based on graph-guided. The experimental results showed that the recall rate of this method was 98.37%, but it had poor adaptability to extreme conditions or new fault patterns [9].

Finding a scientific and effective method to accurately diagnose LB failure types will help provide strong support for LB failure prevention, thereby ensuring the safety of people in the vehicle. Wavelet packet denoising (WPD) is a signal denoising technology based on WP transform [10]. Long short-term memory (LSTM) is a unique type of recurrent neural network that is utilized extensively in domains like power grid prediction and fault diagnostics because of its tremendous flexibility and ability to capture long-term relationships [11]. Many experts have done relevant research. For example, to improve the accuracy of FD of industrial equipment, Li S et al. proposed an interpretable WP kernel constrained convolution network and conducted experiments on bearing data sets. It was found that the network was more robust than the comparison model [12]. Aiming at the difficulty of FD of wind power gearboxes, Zhang T and Wang Y proposed a FD method based on WPD and convolutional neural network. Experimental results showed that the FD accuracy of this method reached 92.24% and 96.16% respectively under strong noise and variable working conditions [13]. Hui H et al. suggested an enhanced WP threshold denoising technique to increase the precision of plunger motor fault detection. According to experimental findings, this technique increased fault detection accuracy [14]. Qin S et al. suggested an FD approach based on enhanced LSTM to address the issue of pitch system defects being hard to identify in time. Results from experiments demonstrated the efficacy of this approach [15]. Ren C et al. proposed an FD model that blended convolutional neural networks and LSTM to address the issue of FD in nuclear power plants. According to experimental findings, this model's recognition rate was 99.6% [16].

The above related results show that the current automotive LB FD method has made certain progress in some aspects. However, there are still problems such as low DA, insufficient fault type classification capabilities, time-consuming calculations, insufficient sensitivity to specific fault types, and poor adaptability under complex working conditions. Therefore, this study introduces the WPD algorithm and LSTM network, and constructs a LB FD algorithm based on the WPD algorithm and LSTM. Moreover, this study aims at the problem of difficult LSTM parameter selection, introduces the gray wolf optimizer (GWO) that combines adaptive strategies and chaotic search strategies to improve it, and constructs an improved GWO-LSTM algorithm for automotive LB FD, aiming to improve the accuracy of automotive LB FD. To clarify this positioning, a paragraph has been added at the end of Section 1. The specific content is as follows. This research aims to integrate mature technologies and address the specific challenges of FD for automotive lithium-ion batteries under complex operating conditions. A tailored diagnostic process is developed to establish a systematically verified diagnostic method. The practical value of this research lies in covering ablation experiments, multi-baseline comparisons, interpretability analysis that connects electrochemical mechanisms with model decisions, robustness assessment under different temperature profiles and aging states, and cross-domain validation of field-collected data.

2. Methods

2.1 Design of LB FD Model based on LSTM

With the popularity of electric vehicles, safety accidents caused by LB failures occur frequently, and the diagnosis of LB failures is particularly important. The study develops a car LB FD approach based on LSTM and WP noise reduction to increase the accuracy of the LB FD method. Since the environment of automobile LBs is complex and there is a lot of noise, this study uses WPD to denoise the signal. It starts by choosing the proper wavelet basis function. Second, the WP coefficients are obtained by breaking down the signal into WPs. The WP coefficients are next subjected to threshold processing, which results in the suppression of noise by setting the WP coefficients smaller than the threshold to zero and keeping the coefficients greater than the threshold. Finally, the signal is reconstructed by WP, and the reconstructed signal is the target signal after noise reduction processing. This study use dB4 as the wavelet basis function and three-level WP (3LWP) decomposition to compute the WP coefficients in order to increase the accuracy of LB FD. One method for analyzing and processing complicated signals is WP decomposition. It decomposes the original signal into multiple coefficients in different frequency bands through layer-by-layer decomposition. Each coefficient represents information about the signal in a specific frequency band and time scale.

The 3LWP decomposition diagram and decomposed wavelet tree are shown in Figure 1 [17].

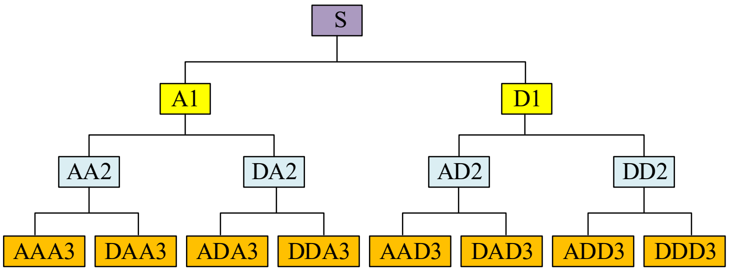

(a) Diagram of three-layer wavelet packet decomposition

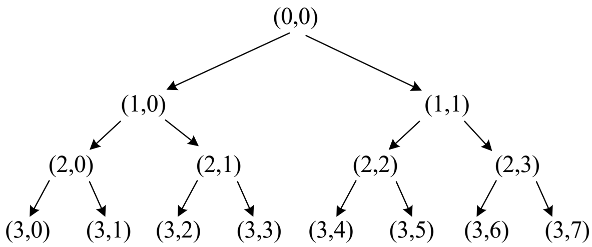

(b) Three-layer wavelet packet decomposition wavelet tree

Figure 1: Schematic diagram of the decomposition of the 3LWP and the decomposed wavelet tree

In Figure 1(a) shows the decomposition process of the 3LWP. First, the original signal S is decomposed into the approximate coefficient $A1$ and the detail coefficient $D1$ of the first layer. Then, $A1$ and $D1$ are respectively decomposed into the coefficients of the second layer, namely $AA2$ and $DA2$, etc. After three levels of decomposition in this process, S is decomposed into coefficients of 8 different frequency bands, namely $AAA3$, $DAA3$, $ADA3$, $AAD3$, $DAD3$, etc. In Figure 1(a), the approximation coefficients include the low-frequency part of the signal, and the detail coefficients include the high-frequency part of the signal. Figure 1(b) shows the coefficient evolution process of the signal from the original state to each level in a tree structure.

Among them, (0, 0) represents the original signal. (1, 0) represents the approximate coefficient of the first layer, and (1,1) represents the detail coefficient of the first layer. (2, 0) is the approximate coefficient of the second layer. (2, 1) and (2, 2) are the detail coefficients of the second layer. In the third layer, (3, 0), (3, 3), and (3, 6) are approximate coefficients, and the rest are detail coefficients. Among them, the WP reconstruction of the signal can be expressed by Equation (1).

$$d_j^n[k]=\sum_m h_{(k-2m)} d_{j+1}^{2n}[m]+\sum_m g_{k-2m} d_{j+1}^{2n+1}[m] \tag{1}$$

In Equation (1), n is the decomposed segment. h_{k-2m} and g_{k-2m} are the coefficients of the reconstructed low-pass filter and high-pass filter. j displays the number of decomposition layers. k and m are translation parameters. $d_j^n[k]$ is the WP coefficient of the reconstructed signal. After WPD, this study uses LSTM network to diagnose LB faults. The LSTM structure and gate functions are shown in Figure 2.

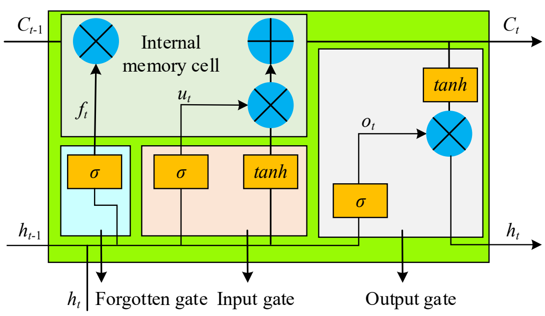

(a) Basic structure of LSTM

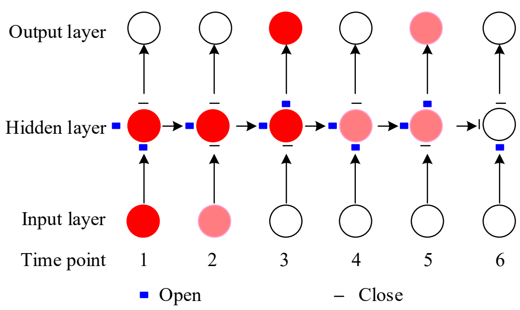

(b) LSTM gate function

Figure 2: LSTM structure and gate function

In Figure 2(a), t is the time step. C_{t-1} and h_{t-1} are the unit state (US) and hidden state (HS) at time step $t-1$. f_t and u_t are the outputs of the forget gate (FG) and the input gate (IG) respectively. o_t is the output of the output gate. C_t and h_t are the US and HS at time step t respectively. σ is the *Sigmiod* activation function. In Figure 2(a), LSTM consists of an IG, an output gate and a FG. Among them, the IG is responsible for regulating the update of information and status and generating a new candidate memory state. The forgetting gate is responsible for deciding whether past information is retained. The output gate is responsible for managing the output from the memory unit. The state of the memory unit and the input signal are processed together through the *tanh* activation function and the element multiplication operation and then sent to the output gate. Memory information is stored and filtered by the internal memory unit. The gate function is shown in Figure 2(b). Pink, red and white respectively represent the gate's sensitivity to data. As color depth increases, the gate becomes more sensitive to data. In Figure 2(b), when the gates of the gate input layer, output layer and hidden layer are all in the open state, the data is output there.

The outputs of the IG, output gate and FG of LSTM are shown in Equation (2).

$$\begin{cases} f_t = \sigma(W_f \cdot [h_{t-1}, Q_t] + b_f) \\ u_t = \sigma(W_u \cdot [h_{t-1}, Q_t] + b_u) \\ o_t = \sigma(W_o \cdot [h_{t-1}, Q_t] + b_o) \end{cases} \tag{2}$$

In Equation (2), W_f is the weight matrix (WM) of the forgetting gate. W_u is the WM of the IG. The WM of the W_o output gate. b_f is the bias vector (BV) of the FG. b_u is the BV of the IG. b_o is the bias of the output gate. Q_t is the input feature vector. The update of cell status can be expressed by Equation (3).

$$\begin{cases} C_t = f_t \odot C_{t-1} + u_t \odot tanh(W_c \cdot [h_{t-1}, Q_t] + b_c \\ h_t = o_t \odot tanh(C_t) \end{cases} \tag{3}$$

In Equation (3), W_c and b_c are the WM and BV of the cell state candidate values, respectively. Therefore, this study combines LSTM and wavelet noise reduction algorithms to establish an automotive LB FD model based on LSTM and WP noise reduction. The structure of the diagnostic model is shown in Figure 3.

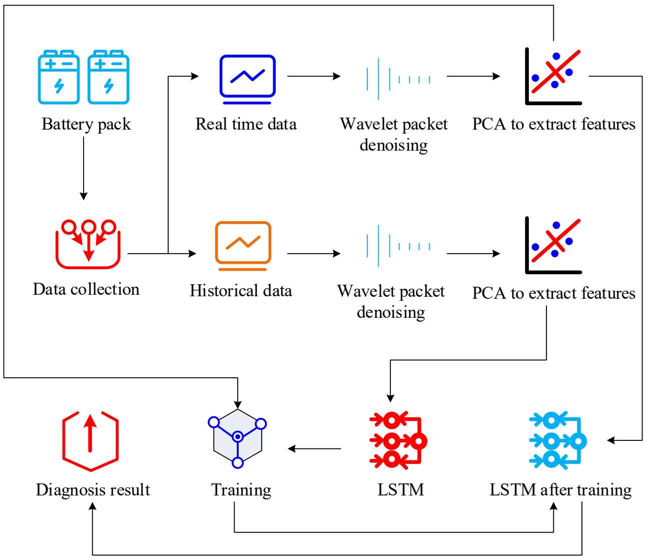

Figure 3: FD model of automotive LB based on LSTM and WPD

In Figure 3, the model diagnosis process is divided into two stages. In the first stage, WPD is used to denoise the normal and fault data of LBs, including voltage, current, temperature, and discharge data. Second, the PCA algorithm is used to extract the signal features after noise reduction. Reducing computing complexity and eliminating redundant features are two benefits of PCA, an unsupervised learning technique. It is widely used in fields such as feature extraction and data dimensionality reduction. By using the PCA approach to extract signal features, superfluous information in the data may be eliminated, increasing FD accuracy. Battery fault categorization is then accomplished through continuous learning after the data is sent into the LSTM network for training. The second stage is to input the battery data collected in real time into the trained LSTM after WPD and PCA feature extraction, and then realize the diagnosis of LB faults through classification and identification.

2.2 Design of Improved GWO-LSTM Algorithm for Automotive LB FD

Although LSTM can achieve FD of automotive LBs, the performance of the LSTM model is highly dependent on parameter selection. Improper parameter selection may lead to under-fitting or over-fitting problems in the model, thereby reducing the accuracy of diagnosis. To solve this problem, this study introduces GWO to improve it. GWO is a group intelligence optimization method that can more effectively compensate for LSTM's drawbacks due to its powerful global search capability (GSC) and straightforward structure. The GWO algorithm solves optimization problems by imitating gray wolf social behavior and hunting strategies.

The updated schematic diagram of the gray wolf's social hierarchy pyramid and hunting position is shown in Figure 4.

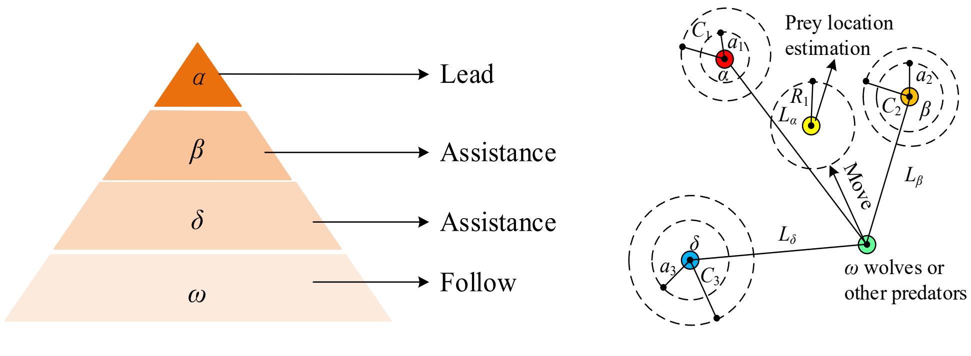

(a) Wolf pack Hierarchy pyramid (b) GWO location update diagram

Figure 4: The hierarchical pyramid of the gray Wolf and the updated position during hunting

In Figure 4(a), wolf α has the highest social rank. Wolf β and wolf δ are next in level. Wolf ω is the lowest level. When hunting, the wolf α is the leader. Wolf β and wolf δ are responsible for assisting. Wolf ω follows the first three. Wolves of all levels work together to surround, hunt and attack prey. The encirclement stage is shown in Equation (4).

$$\begin{cases} \vec{L} = \left|\vec{C}\cdot\vec{X}_P(q) - \vec{X}(q)\right| \\ \vec{X}(q+1) = \vec{X}_P(q) - \vec{Z}\cdot\vec{L} \end{cases} \tag{4}$$

In Equation (4), $\vec{X}(q+1)$ and $\vec{X}(q)$ are the position vectors (PVs) of the prey in the q and $q+1$ iterations, respectively. $\vec{L}$ is the distance vector between the wolf pack and the prey. $q+1$ is the PV of the prey in the q iteration. Z and C are collaborative vectors, and $\vec{Z} = 2\vec{Z}\cdot\vec{r}_1 - \vec{a}$. a is the convergence factor. $\vec{r}_1$ is a random vector, and $\vec{r}_1 \in [0,1]$. $\vec{C} = 2\vec{r}_2$, $\vec{r}_1$ are random vectors, and $\vec{r}_1 \in [0,1]$. Figure 4(b) displays the location update when the wolves are hunting. a_1, a_2, and a_3 are the current optimal directions of wolf α, wolf β and wolf δ. $\vec{L_\alpha}$ is the distance vector between the wolf α and its prey. $\vec{L_\beta}$ is the distance vector between wolf β and prey. $\vec{L_\delta}$ is the distance vector between wolf δ and prey. R_1 is the maximum step length of one movement of the target individual (gray wolf). $\vec{C_1}$, $\vec{C_2}$, and $\vec{C_3}$ are collaborative vectors. In Figure 4(b), while hunting, the position of the wolves is changing, and the distance between the gray wolf and the prey is also changing. Meanwhile, the wolves guide ω movement through wolf α, wolf β, and wolf δ to achieve global optimization, then the distance vectors between wolf α, wolf β, and wolf δ and their prey can be expressed by Equation (5).

$$\begin{cases} \vec{L_\alpha} = \left|\vec{C_1} - \vec{X_\alpha} - \vec{X}\right| \\ \vec{L_\beta} = \left|\vec{C_2} - \vec{X_\beta} - \vec{X}\right| \\ \vec{L_\delta} = \left|\vec{C_3} - \vec{X_\delta} - \vec{X}\right| \end{cases} \tag{5}$$

In Equation (5), $\vec{X_\alpha}$, $\vec{X_\beta}$, and $\vec{X_\delta}$ are the current PVs of wolf α, wolf β, and wolf δ. $\vec{X}$ is the current PV of the gray wolf. The current gray wolf is the gray wolf that needs to be calculated with the wolf α, wolf β, and wolf δ. When $|Z|>1$, wolves disperse in various areas searching for prey. During $|Z|<1$, the wolves focus on searching for prey in a certain area. During this process, the wolf ω are guided by the wolf α, wolf β, and wolf δ to update their positions, as shown in Equation (6).

$$\vec{X_\omega}(q+1) = (\vec{X_1} + \vec{X_2} + \vec{X_3}) \tag{6}$$

In Equation (6), $\overrightarrow{X_{\omega}}(q+1)$ is the PV of ω at the $q+1$ th iteration. $\overrightarrow{X_1}$, $\overrightarrow{X_2}$, and $\overrightarrow{X_3}$ are the intermediate PVs generated by the target gray wolf guided by wolf α, wolf β, and wolf δ, as shown in Equation (7).

$$\begin{cases} \overrightarrow{X_1} = \overrightarrow{X_\alpha} - \overrightarrow{Z_1} \cdot \overrightarrow{L_\alpha} \\ \overrightarrow{X_2} = \overrightarrow{X_\beta} - \overrightarrow{Z_2} \cdot \overrightarrow{L_\beta} \\ \overrightarrow{X_3} = \overrightarrow{X_\delta} - \overrightarrow{Z_3} \cdot \overrightarrow{L_\delta} \end{cases} \tag{7}$$

In Equation (7), $\overrightarrow{X_1}$, $\overrightarrow{X_2}$, and $\overrightarrow{X_3}$ are vectors that control the step length and direction of position update of wolf α, wolf β, and wolf δ. When updating the step size, the GWO algorithm updates the step size by dynamically adjusting the position of the gray wolves in the wolf pack, which can be calculated using formula $\varphi = 2 - 2q/T$. Among them, φ is the control parameter, which decreases from 2 to 1 as the quantity of iterations increases. T is the maximum quantity of iterations. To improve the convergence speed of the GWO algorithm, this study introduces an adaptive strategy to improve its control parameters. The improved control parameters can be expressed by Equation (8).

$$\varphi_i = \begin{cases} \varphi_{min} + \dfrac{(\varphi_{max} - \varphi_{min}) \cdot (J_i - J_{min})}{(J_{arg} - J_{min})}, J_i \le J_{arg} \\ \varphi_{max}, \qquad J_i > J_{arg} \end{cases} \tag{8}$$

In Equation (8), φ_{min} and φ_{max} are the minimum and maximum values of φ, respectively. J_{arg} is the average fitness of the current group. J_i is the fitness of the current individual. J_{min} is the minimum fitness of the current group. φ_i is the control parameter value of the current individual. Through intelligent adaptation strategies, the search area of wolf individuals can be enlarged and moved closer to a better search area. Then, the position is updated according to the improved control parameters, and the prey position $x(q+1)$ is shown in Equation (9).

$$x(q+1) = \frac{(\frac{J_\alpha}{J_\delta})x_1 + (\frac{J_\beta}{J_\delta})x_2 + x_3}{3} \tag{9}$$

In Equation (9), J_α, J_β, and J_δ are the fitness values of wolf α, β, and δ, respectively. x_1, x_2, and x_3 are the positions of wolf α, β, and δ, respectively. This work employs a chaotic search approach to increase the algorithm's population variety in order to improve the GWO algorithm's capacity to escape the local optimum. Chaos search strategy is a heuristic search algorithm that uses chaos theory to enhance the GSC of the optimization algorithm and avoid falling into the local optimal solution. Its process is utilized to increase population diversity in the GWO algorithm. First, when the iteration counter counts to 0, the decision variables are mapped to chaos variables, as shown in Equation (10).

$$\phi_\gamma^v = \frac{\chi_\gamma^v - \chi_{min,\gamma}}{\chi_\gamma^v - \chi_{max,\gamma}} \tag{10}$$

In Equation (10), ϕ_γ^v is a chaotic variable, and $\phi_\gamma^v \in [0,1]$. χ is the decision variable. $\chi_{min,\gamma}$ and $\chi_{max,\gamma}$ are the upper and lower search limits of the γ th dimension variable of χ, respectively. v is the number of chaos iterations. Second, iterative calculation of chaotic variables is carried out, that is, iterative calculation of chaotic variables is performed for local search. The chaos variable ϕ_γ^{v+1} after $v+1$ iterations is shown in Equation (11).

$$\phi_\gamma^{v+1} = 4\phi_\gamma^v(1-\phi_\gamma^v) \tag{11}$$

Finally, ϕ_γ^{v+1} is converted into decision variable χ_γ^{v+1}, as shown in Equation (12).

$$\chi_\gamma^{v+1} = \chi_{min,\gamma} + \phi_\gamma^{v+1}(\chi_{max,\gamma} - \chi_{min,\gamma}) \tag{12}$$

During the execution phase, the algorithm can continuously determine whether the updated solution is superior to the initial solution by using the chaotic search approach. If it is or reaches the termination condition, the solution is regarded as the final solution. Otherwise, continue iterating until the conditions are met.

As a result, the GWO algorithm improvement is completed. The improved GWO algorithm flow is shown in Figure 5.

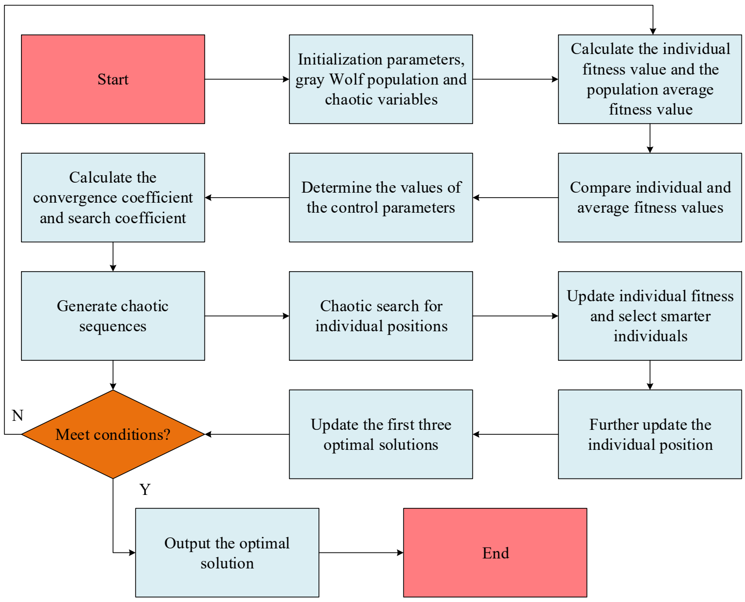

Figure 5: Improves the GWO algorithm process

The enhanced GWO algorithm's phases are shown in Figure 5. Initially, the study sets parameters like population size and iteration count. Additionally, it sets the gray wolf population's position and chaotic variables to their initial values. Second, each gray wolf's fitness value is computed, and the population's average fitness is ascertained. Then, the fitness of each gray wolf is compared with the average fitness to dynamically adjust the control parameters. Next, the convergence coefficient and search coefficient are calculated. Then, a chaotic sequence is generated, and the chaotic sequence is used to conduct chaotic search for individual positions. Meanwhile, individual fitness is updated and better individuals are selected.

Then, the individual position is further updated, and the first three optimal solutions, namely the optimal solutions represented by α, β, and δ, are updated. Lastly, the study outputs the best solution and terminates the algorithm after determining whether the termination conditions—such as reaching the maximum number of iterations or discovering a good solution—have been satisfied. Otherwise, continue iterating until the optimal solution is found. Finally, the improved GWO algorithm and LSTM network are combined to construct an improved GWO-LSTM algorithm.

The operation steps of this algorithm are shown in Figure 6.

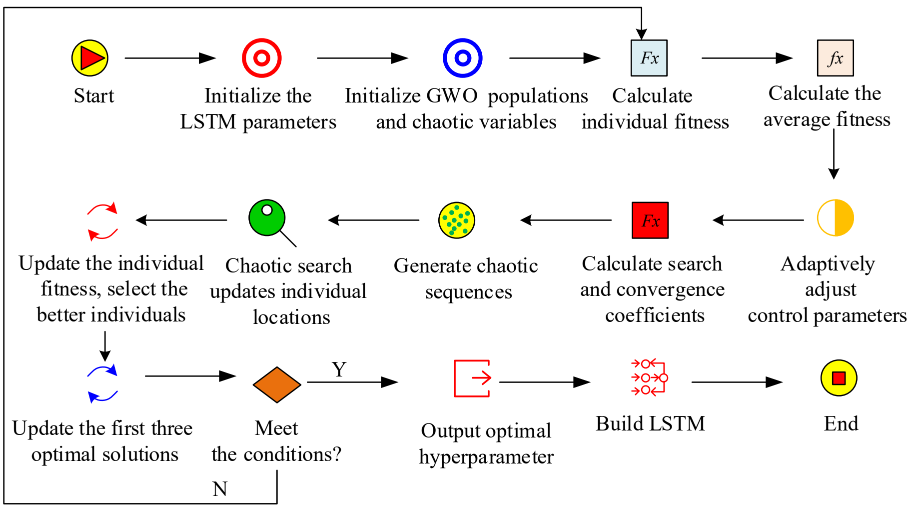

Figure 6: Steps of the improved GWO-LSTM algorithm

In Figure 6, the algorithm steps first initialize the weights, biases and other parameters of the LSTM network. Moreover, it initializes the population and chaotic sequence of the GWO algorithm. Each individual in the population represents a set of LSTM parameter combinations. Second, it calculates the fitness value, which is the mean square error of LSTM on the validation set. Meanwhile, the average fitness value is calculated. Then, the convergence coefficient and search coefficient are calculated, and a chaotic sequence is generated, and the individual position is updated through the chaotic sequence. Furthermore, it updates the individual fitness value to select a better individual. Meanwhile, the first three optimal individuals (that is, the optimal solutions represented by α, β, and δ wolves) are updated as the optimal solution. Next, ascertain if the termination requirement is satisfied. If satisfied, the hyperparameters are output, the LSTM model is constructed using the hyperparameters, and the algorithm ends. Otherwise, it iterates again until the conditions are met. Eventually, the original FD model will be replaced by an improved GWO-LSTM algorithm and trained using historical LB data. Moreover, using the new data set, FD can be completed. In this model, the PCA transformation decomposes the input features into two main components. Among them, PC1 captures the electrochemical behavior through changes in voltage and charging status, while PC2 separates the thermodynamic aspects through temperature-related features. This decomposition ensures that the dimensionality reduction process retains the physical meaning rather than being a random projection. In the LSTM layer, the forget gate selectively retains historical information related to the progressive degradation pattern, while the input gate is activated strongly when instantaneous deviations (such as rapid voltage drop or sudden temperature rise) indicate an impending failure. The output gate then integrates these temporal contexts to generate diagnostic decisions. In this study, the improved GWO algorithm is employed to optimize six key hyperparameters of the LSTM network. These hyperparameters include the number of hidden units within the search interval of 50 to 200, the initial learning rate ranging from 0.0001 to 0.01, the batch size varying between 16 and 128, the time-step length set from 10 to 50, the dropout rate constraines within 0.1 to 0.5, and the maximum training epochs bounded between 50 and 300. Each individual in the gray wolf population represents a specific combination of the above parameters, and the fitness value is defined as the mean squared error of the LSTM model on the validation set.

Regarding the interface between PCA and the temporal LSTM, the original 12-dimensional feature vector is first projected onto the principal component space, yielding two principal components denoted as PC1 and PC2. A sliding window with a length of 20 and a step size of 1 is then applied to the PCA-reduced feature sequence. Consequently, the input tensor feed into the LSTM network possessed dimensions of 20 by 2, where each row correspond to the PCA feature vector at a particular time step and each column represent one principal component.

This sliding-window mechanism ensures that the temporal dependencies among consecutive sampling points are preserved while the redundant information is eliminated through PCA dimensionality reduction.

3. Results and Analysis

3.1 Improved GWO-LSTM Performance Analysis

After constructing the improved GWO-LSTM algorithm, this study compared its performance with the PSO-SVM algorithm, CNN-LSTM algorithm, and GA-BP algorithm. For the GWO parameter settings, the initial population size was 50, and the convergence factor interval was [0, 2]. For the LSTM algorithm parameter settings, the initial learning rate was 0.001, and the initial weight interval was [-0.5, 0.5]. The input layer and hidden layer nodes were 4 and 2 respectively, the quantity of output layer nodes was 8, and the optimizer was Adam. The quantity of iterations of the algorithm was 300, and the five-fold crossover method was used for tuning, and the early stopping mechanism prevented overfitting. The normal and fault states of LBs were normal (A), low capacity (B), high internal resistance (C), and low remaining power of the battery (D). The corresponding neuron states were [1;0;0;0], [0;1;0;0], [0;0;1;0], [0;0;0;1]. The data came from the large-scale lithium-ion battery dataset of new energy vehicles. This dataset contained real-world operational data collected from multiple electric vehicle models under various driving conditions, including urban roads, highways, and mixed scenarios. The voltage measurement used a sensor with an accuracy of 0.1% of the full scale (FS), while the temperature sensor had an accuracy of ±0.5°C. The signal-to-noise ratio (SNR) of the original signal ranged from 30 to 45 decibels. In terms of the nature of the faults, 12% of the fault instances were actual operational faults identified from the field data, and 88% were laboratory faults generated under controlled conditions. This dataset covered a wide working temperature range of -10°C to 45°C and encompassed 50 to 1200 equivalent full cycles of battery aging states, corresponding to state of health levels (SOH) ranging from 95% to 80%. The dataset encompasseed four years of operational records (2019-2022) with a sampling frequency of 1 Hz.

Each data record included 12 raw features: voltage, current, temperature, state of charge (SOC), and other battery management system (BMS) parameters. The access address was: http://ivstskl.changan.com.cn/?p=2697. A total of

19,882 pieces of data were selected, 80% of which were training sets, 10% were test sets, and 10% were validation sets. The dataset distribution across fault categories was as follows: normal state (A): 8,450 samples (42.5%), low capacity (B): 4,320 samples (21.7%), high internal resistance (C): 3,612 samples (18.2%), and low remaining power (D): 3,500 samples (17.6%), ensuring a relatively balanced representation of all fault types. Data preprocessing first removed missing values and outliers, and used linear function normalization method to normalize the original data to the [0,1] range. Second, the wavelet denoising method was used to remove noise.

Finally, the PCA algorithm was used to extract features. Comparison indicators included accuracy, recall, F1 score, etc. Table 1 depicts the experimental setting.

Table 1. Experimental environment configuration

Parameter names	Parameter
CPU	Intel Core i9-12900K
Main frequency	5.2GHz
RAM	32GB
HDC	1TB
Operating system	Windows 10 64
Matlab version	Matlab 2021a

In the above environment, this study first put the proposed algorithm into different data sets to conduct ablation experiments. Table 2 displays the outcomes of the experiment.

Table 2. Results of the ablation experiment

Dataset	Indicator	LSTM	GWO+LSTM	Adaptive strategy +GWO+LSTM	Improve GWO-LSTM
CALCE dataset	AUC value	0.763	0.849	0.892	0.967
	Number of convergent iterations	273	196	126	53
	Loss value	0.487	0.362	0.257	0.134
A large-scale dataset of lithium-ion batteries for new energy vehicles	AUC value	0.754	0.836	0.884	0.958
	Number of convergent iterations	0.493	181	128	57
	Loss value	0.698	0.359	0.266	0.126

Table 2 displays that the study's enhanced GWO-LSTM method outperforms the pre-improved LSTM algorithm in terms of AUC value, convergence iteration number, and loss value. Moreover, it maintained good performance in different data sets. This demonstrated the good improvement effect and good generalization capabilities of the algorithm suggested in this study. The comparative experimental results of accuracy, F1 score, recall rate, and precision rate are shown in Figure 7.

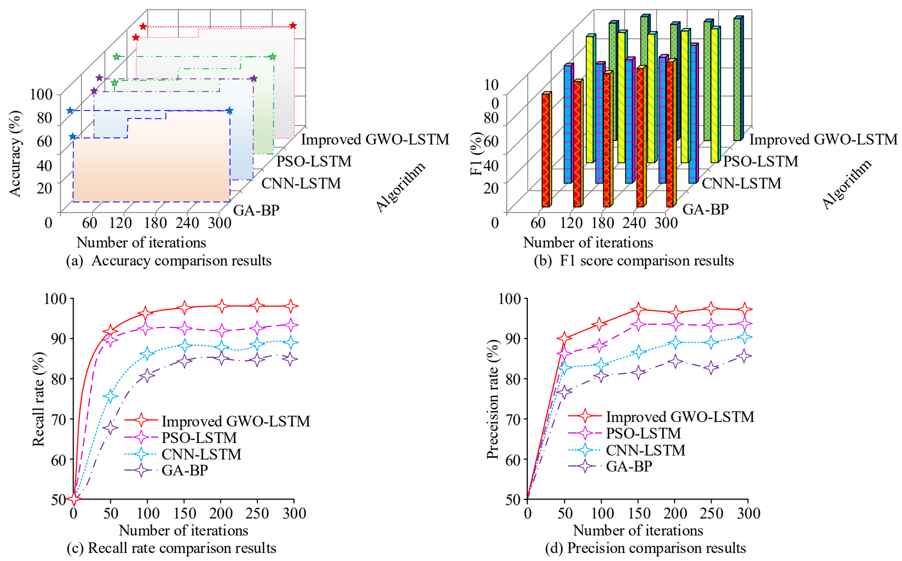

Figure 7: Comparison results of accuracy rate, F1 score, recall rate and precision rate

In Figure 7(a), the accuracy of the improved GWO-LSTM algorithm was 98.16%, which was significantly higher than PSO-SVM's 88.13%, CNN-LSTM's 86.79%, and GA-BP's 84.28%. The study's enhanced GWO-LSTM algorithm had the best accuracy. In Figure 7(b), the F1 scores of the improved GWO-LSTM, PSO-SVM, CNN-LSTM, and GA-BP proposed by the study were 97.69%, 89.46%, 85.78%, and 83.29%. The study's enhanced algorithm had the greatest F1 score. In Figure 7(c), the recall rates of the improved GWO-LSTM, PSO-SVM, CNN-LSTM, and GA-BP algorithms were 98.03%, 91.23%, 88.87%, and 85.77%.

The study's enhanced GWO-LSTM algorithm had the best recall rate.

In Figure 7(d), the improved GWO-LSTM algorithm proposed in the study had the highest recall rate, with a value of 97.86%. It was much higher than 89.87% of PSO-SVM, 87.61% of CNN-LSTM and 84.85% of GA-BP. The aforementioned findings demonstrated that the study's enhanced algorithm outperformed the compared algorithms in terms of accuracy, F1 score, recall rate, and precision rate. Figure 8 displays the mean absolute error (MAE) and root mean squared error (RMSE) comparative findings for each algorithm.

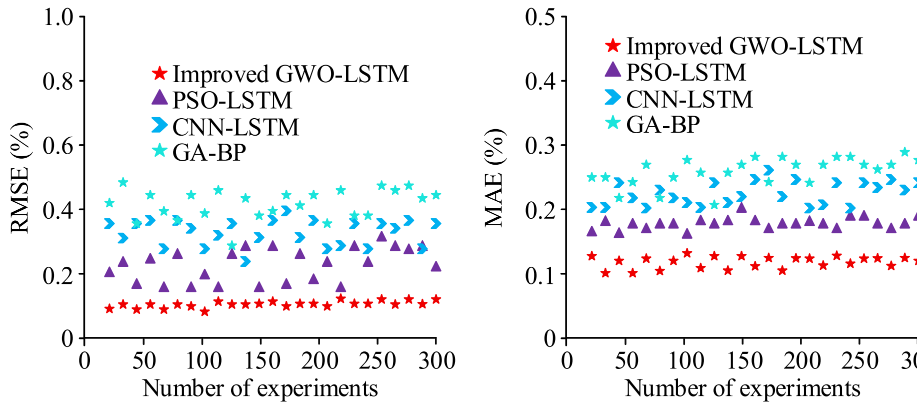

(a) RMSE comparison results (b) MAE comparison results

Figure 8: Comparison results of RMSE and MAE

In Figure 8(a), the RMSE values of the improved GWO-LSTM, PSO-SVM, CNN-LSTM, and GA-BP algorithms were 0.13%, 0.2%, 0.38%, and 0.42%, respectively. The study's enhanced GWO-LSTM algorithm had the lowest RMSE value. In Figure 8(b), the MAE value of the improved GWO-LSTM algorithm proposed in the study was 0.09%, which was significantly lower than 0.16% of PSO-SVM, 0.23% of CNN-LSTM, and 0.26% of GA-BP. In summary, the proposed algorithm achieved the lowest RMSE and MAE among all comparison methods. To further evaluate the performance of the proposed algorithm, the study conducted a performance comparison analysis by comparing the proposed algorithm with Transformer, Physics-informed Neural Network (PINN), XGBoost + LSTM, Random Forest integration, and GNN for battery cell correlation methods. The assessment results are shown in Table 3.

Table 3. Evaluation results

Indicators	Transformer	PINN	XGBoost+LSTM	GNN	Research
Running time	3245.8s	2876.4s	1567.3s	4123.5s	1245.6s
Memory usage	256.4MB	198.7MB	89.5MB	312.6MB	45.2MB
Model size	512.0KB	384.5KB	156.3KB	640.8KB	128.0KB
Floating-point operation volume	15.6MFLOPs	12.3MFLOPs	4.8MFLOPs	18.9MFLOPs	2.3MFLOPs
Embedded feasibility	N	N	Y	N	Y

From Table 3, the running time, memory usage, model size and floating-point operation volume of the algorithm proposed in this study were 1245.6 seconds, 45.2MB, 128.0KB and 2.3 MFLOPs, respectively, all of which were superior to those of the comparison methods. Moreover, it had good embedding feasibility. The above results indicated that the algorithm proposed in this study had good performance and was superior to the existing algorithms in multiple aspects. To address the "black box" characteristic issue of this model, the research conducted an interpretability analysis from three aspects: PCA component decoupling, SHAP feature contribution, and LSTM gate activation mechanism. The comprehensive results are shown in Table 4.

Table 4. SHAP Feature Importance Analysis

Component	Metric/Feature	Value	Physical Interpretation
PCA	PC1 variance (electrochemical)	62.3%	Voltage,SOC variations
	PC2 variance (thermal)	21.7%	Temperature dynamics
SHAP	Voltage drop rate	0.312	Low capacity (B)
	Temperature rise	0.278	High internal resistance(C)
	SOC inconsistency	0.198	Low SOC(D)
	Current integral	0.145	Low capacity (B)
	Surface temperature	0.067	All types
LSTM Gate	Input gate activation (fault vs. normal)	5.2	Selective attention to deviations
	Forget gate retention (normal state)	0.85	Preserves stable patterns

From Table 4, the interpretability analysis revealed three key findings. First, the PCA transformation effectively decoupled the input features into physically meaningful domains: PC1 (62.3% variance) captured electrochemical behavior through voltage and SOC variations, while PC2 (21.7% variance) isolated thermal dynamics. This decomposition ensured that dimensionality reduction retained clear physical interpretability rather than arbitrary projections. Second, SHAP analysis demonstrated that voltage drop rate (0.312) and temperature rise (0.278) were the dominant contributors to FD decisions, jointly accounting for the majority of prediction importance. These top-ranked features aligned with established battery degradation mechanisms—voltage dynamics indicated capacity fade, while thermal anomalies signaled internal resistance growth. Third, LSTM gate activation patterns confirmed selective temporal processing: the input gate exhibited 5.2× higher activation during fault detection, enabling the model.

To capture instantaneous deviations such as rapid voltage drops or temperature spikes, whereas the forget gate maintained high retention (0.85) for normal states to preserve stable historical patterns. Collectively, these results demonstrated that the IGWO-LSTM model's decisions were traceable to physically interpretable electrochemical-thermal principles, addressing the black-box concern. To eliminate the influence of random initialization on experimental reliability, ten independent runs were carried out for each algorithm with different random seeds. The mean and standard deviation of accuracy, F1 score, recall, and precision were recorded. Moreover, the Wilcoxon signed-rank test was adopted to verify whether the performance gap between the proposed method and each comparison algorithm reached statistical significance. The statistical results are listed in Table 5.

Table 5. Statistical test results

Algorithm	Accuracy (%)	F1 Score (%)	Recall (%)	Precision (%)	p-value
IGWO-LSTM	98.16±0.18	97.69±0.21	98.03±0.17	97.86±0.19	/
PSO-SVM	88.13±0.42	89.46±0.38	91.23±0.45	89.87±0.41	p<0.01
CNN-LSTM	86.79±0.55	85.78±0.52	88.87±0.48	87.61±0.50	p<0.01
GA-BP	84.28±0.61	83.29±0.58	85.77±0.63	84.85±0.59	p<0.01

Table 5 shows that the IGWO-LSTM algorithm attained the highest mean accuracy of 98.16% with a standard deviation of only 0.18%, outperforming PSO-SVM, CNN-LSTM, and GA-BP in all four metrics. The standard deviations of the proposed method remained below 0.21%, indicating superior stability. Wilcoxon signed-rank tests yielded p-values below 0.01 for all pairwise comparisons, confirming that the performance improvements were statistically significant. To further verify the diagnostic capability under authentic field degradation patterns, a cross-domain validation was conducted on the BattGP dataset. This open-source dataset contained 28 sets of 24 V LFP energy storage battery packs returned under manufacturer warranty after long-term user operation, with all faults collected entirely from field conditions without artificial injection. The dataset was publicly available at https://zenodo.org/records/13715694 and an accompanying Python toolkit was provided at https://github.com/shiyunliu-battery/Iontech.

Although these batteries were deployed in stationary storage rather than electric vehicles, the underlying electrochemical degradation mechanisms were fundamentally similar to those in automotive LBs. For fair comparison, all methods were tuned with the same five-fold cross-validation strategy. The IGWO-LSTM model employed a GWO population of 50 and 300 iterations, optimizing six LSTM hyperparameters including hidden units, learning rate, batch size, time-step length, dropout rate, and training epochs within their respective search intervals.

For the Transformer baseline, 4 encoder layers with 8 attention heads, d_model of 128, and the AdamW optimizer were adopted. The XGBoost+LSTM baseline combined 200 XGBoost estimators with an LSTM branch of 100 hidden units. The GNN baseline used 2 GCN layers with 64 hidden units and a cell-correlation adjacency matrix. The PINN baseline deployed 3 fully-connected layers with a physics constraint coefficient of 0.01. The Random Forest baseline was configured with 500 estimators and a maximum depth of 20. Ten independent runs with distinct random seeds were performed for each method. The statistical results are listed in Table 6.

Table 6. Cross-domain validation results on the BattGP field-collected dataset

Algorithm	Accuracy (%)	F1 Score (%)	Recall (%)	Precision (%)	*p*-value
IGWO-LSTM	95.42±0.32	94.83±0.35	95.18±0.31	94.51±0.37	/
Transformer	92.15±0.58	91.32±0.62	92.47±0.56	90.21±0.65	$p<0.01$
XGBoost+LSTM	91.48±0.55	90.55±0.59	91.62±0.53	89.51±0.62	$p<0.01$
GNN	90.76±0.63	89.91±0.67	91.05±0.61	88.80±0.70	$p<0.01$
PINN	89.68±0.71	88.85±0.74	90.12±0.69	87.63±0.77	$p<0.01$
RandomForest	87.23±0.82	86.14±0.85	88.37±0.79	84.02±0.88	$p<0.01$

Table 6 shows that the IGWO-LSTM model achieved the highest accuracy of 95.42% with a standard deviation of merely 0.32% on the BattGP field-collected dataset, outperforming Transformer, XGBoost+LSTM, GNN, PINN, and Random Forest. Wilcoxon signed-rank tests yielded p-values below 0.01 for all pairwise comparisons, confirming statistically significant advantages. The proposed model maintained a superior margin of at least 3.27 percentage points over the strongest baseline under authentic field degradation conditions, demonstrating robust cross-domain generalization capability.

3.2 Analysis of the Application Effect of FD Model

This study examines the application effect of the suggested LB FD model based on enhanced GWO-LSTM after confirming the performance of the suggested improved GWO-LSTM algorithm. In a car LB repair center, 600 faulty LBs were randomly selected for diagnosis. The comparative diagnosis models were PSO-SVM model, CNN-LSTM model, and GA-BP model.

Figure 9 displays a comparison of each model's diagnostic results' fitting degree.

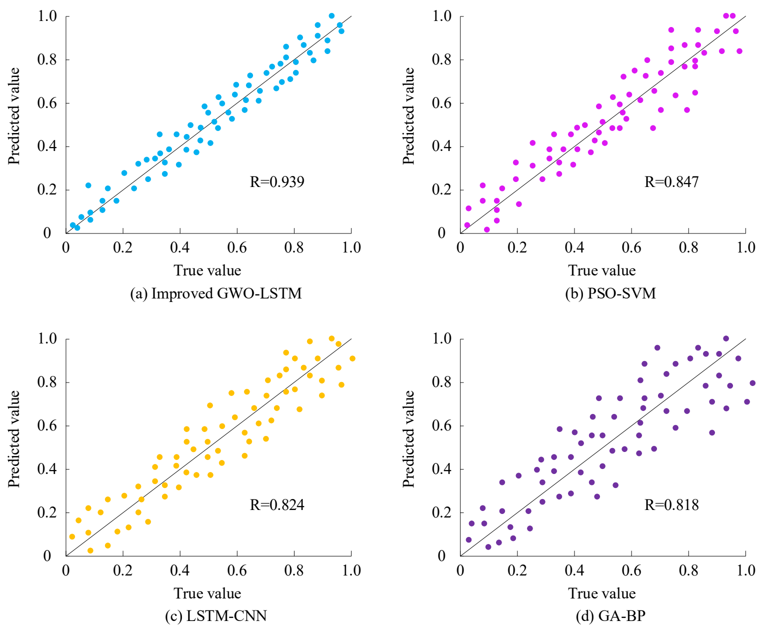

Figure 9: Comparison of the fit of the diagnostic results of each model

In Figure 9(a), the fitting coefficient of the proposed improved GWO-LSTM model was 0.939, which was higher than the 0.847 of the PSO-SVM model of Figure 9(b), the 0.824 of the LSTM-CNN model of Figure 9(c), and the 0.818 of the GA-BP model of Figure 9(d).

In summary, judging from the fitting results, the diagnosis results of the LB FD model proposed in the study were closest to the real results. It performed better compared to the comparison model. The DA of each model for the four types of faults is shown in Figure 10.

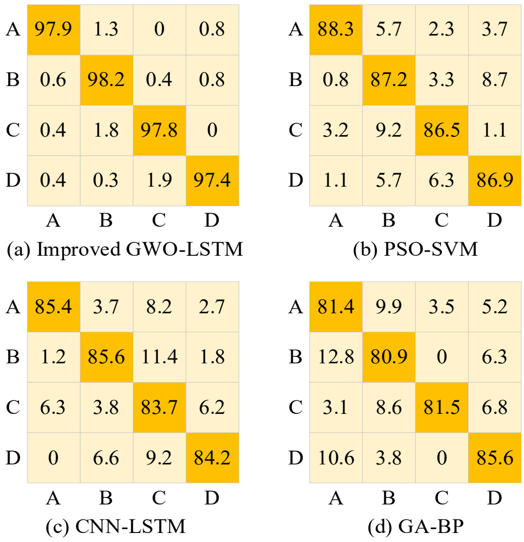

Figure 10: DA results of each model for the four faults

In Figure 10(a), the DA of the improved GWO-LSTM model proposed in the study was 97.9%, 98.2%, 97.8%, and 97.4% respectively for normal (A), low capacity (B), large internal resistance (C), and low remaining battery power (D). It was higher than the highest value of 88.3% for the PSO-SVM model in Figure 10(b), 85.6% for the CNN-LSTM model in Figure 10(c), and 89.9% for the GA-BP model in Figure 10(d). In summary, the model suggested in the study outperformed the comparative model, according to the DA results of the four fault kinds. To further verify the performance of the proposed method in the research, it was applied under complex working conditions for an effectiveness analysis. The analysis results are shown in Table 7.

Table 7. Diagnostic results under complex conditions

Scenario	Condition	Accuracy	F1 Score	Key Finding
Temperature profiles	Low (-10°C)	94.22%	93.89%	Reduced ionic conductivity affects voltage features
	Standard (25°C)	98.27%	97.78%	Baseline optimal performance
	High (45°C)	95.65%	95.14%	Accelerated side reactions increase noise
Usage conditions	Urban cycle	96.84%	96.33%	Frequent regenerative braking aids diagnosis
	Highway cycle	93.53%	92.94%	Sustained high current reduces feature diversity
	Mixed cycle	97.47%	97.65%	Balanced performance across driving patterns
Aging states	Early (SOH 95%)	97.98%	97.57%	Fault signatures subtle but detectable
	Mid (SOH 87%)	98.16%	97.89%	Optimal fault-manifestation window
	Late (SOH 80%)	89.34%	88.18%	Severe degradation masks fault distinctions
Multi-fault	B+C (capacity+resistance)	85.63%	84.24%	Overlapping symptoms reduce separability
	B+D (capacity+SOC)	91.41%	90.85%	Partial feature overlap manageable
	C+D (resistance+SOC)	88.72%	87.50%	Thermal-SOC coupling introduces ambiguity

From Table 7, the expanded testing reveaed three critical patterns regarding the model's robustness under complex operating conditions. First, temperature variations moderately degraded diagnostic performance: accuracy drops to 94.22% at -10 ° C due to reduced ionic conductivity distorting voltage features, while high temperature (45° C) caused a smaller decline to 95.65% through accelerated side reactions increasing signal noise. This asymmetry indicated cold environments pose greater challenges than heat for the proposed algorithm. Second, usage conditions substantially affected reliability: highway cycling reduced accuracy to 93.53%—the lowest among single-factor scenarios — because sustained high current diminished feature diversity, whereas urban cycling (96.84%) benefited from frequent regenerative braking that enriched diagnostic signatures. Third, aging exhibited a nonlinear impact: mid-life batteries (SOH 87%) achieve optimal performance (98.16%), but severe aging (SOH 80%) caused significant degradation (89.34%) as compounded capacity fade masks fault-specific characteristics. Most critically, multi-fault scenarios exposed the fundamental limitation: When capacity degradation coincided with high internal resistance (B+C), accuracy plummets to 85.63%, demonstrating that overlapping fault mechanisms exceed the current feature engineering capacity. While B+D (91.41%) and C+D (88.72%) combinations remained partially separable, the B+C overlap presented the primary barrier to real-world deployment. These results validated that the IGWO-LSTM model maintained satisfactory robustness across individual complex conditions.

4. Discussion

The superior performance of the improved GWO-LSTM algorithm can be attributed to the synergistic effect of three mechanisms. First, the adaptive control parameter strategy dynamically adjusts the search behavior based on the relative fitness of each grey wolf individual. When the individual fitness is better than the population average, the control parameter decreases to strengthen local exploitation. Otherwise, it increases to maintain global exploration. This mechanism prevents the premature convergence that commonly occurs in standard GWO when solving high-dimensional LSTM hyperparameter optimization problems. Second, the chaotic search strategy introduces population diversity through logistic map iteration when the algorithm approaches local optima. The chaotic variable traversal covers regions that the deterministic wolf position update may miss, thereby improving the probability of escaping suboptimal LSTM configurations. Third, the integration of WPD and principal component analysis forms an effective preprocessing pipeline. WP decomposition separates the battery voltage, current, and temperature signals into multiple frequency bands, and the threshold processing suppresses high-frequency measurement noise while retaining low-frequency fault trend components. Principal component analysis subsequently projects the denoised features onto orthogonal axes that maximize variance, eliminating redundant correlations among the original 12-dimensional inputs. This ensures that the LSTM network receives temporally coherent and dimensionally compact inputs, which is particularly beneficial for capturing the long-term degradation patterns of LBs.

The comparison with existing literature further supports the above analysis. The accuracy improvement achieved in this study is consistent with the findings of Lu Y et al. [18], who demonstrated that adaptive switching strategies enhance the exploitation capability of grey wolf optimizer variants in complex search spaces. The effectiveness of chaotic search in preventing local stagnation aligns with the results reported by Lawah A. I. et al. [19]. The error reduction observed in this study is comparable to the outcomes of Ma C et al. [20], who employed GWO to optimize LSTM parameters for traffic flow prediction and reported significant forecasting error reduction. The application effect of the FD model is in line with the work of Pang J et al [21], who combined WPD with LSTM for water quality prediction and verified the robustness of this preprocessing-network architecture under noisy field conditions.

Nevertheless, this study is subject to certain limitations. Although the BattGP field-collected dataset is employed for cross-domain validation and the proposed model achieved satisfactory accuracy on authentic operational degradation data, the domain gap between stationary energy storage systems and automotive power batteries remains. The electrochemical degradation mechanisms are similar, yet the dynamic load profiles, vibration coupling, and thermal management strategies differ substantially between the two application scenarios. In addition, the 12% real-world vehicle data reserved in the primary dataset constitute a relatively small proportion, which may not fully capture the full spectrum of stochastic driving conditions. Future investigations will focus on expanding the proportion of field-collected automotive operational data, constructing domain adaptation strategies to bridge the distribution gap between laboratory and field samples, and incorporating multi-physical coupling effects to improve practical applicability.

5. Summary

This study developed an automotive LB FD model based on WPD, principal component analysis, and an improved grey wolf optimization-LSTM network. The proposed algorithm achieved an accuracy of 98.16% and an F1 score of 97.69% on the primary dataset, and maintained satisfactory performance on an independent field-collected validation subset. The model exhibited low computational cost, small memory footprint, and good embedded feasibility, which supported its practical deployment in battery management systems. The main limitation lies in the high proportion of laboratory-generated fault data, which might constrain generalization under highly complex real-world driving scenarios. Future work will focus on expanding field-collected data proportion and developing domain adaptation strategies to bridge the gap between controlled experiments and actual operating conditions.

Reference

[1] Wu, Z., Zhao, Y., & Zhang, N. (2023). A literature survey of green and low-carbon economics using natural experiment approaches in top field journal. *Green and Low-Carbon Economy*, *1*(1), 2–14. https://doi.org/10.47852/bonviewGLCE3202827

[2] Guo, X., Sun, Y., & Ren, D. (2023). Life cycle carbon emission and cost-effectiveness analysis of electric vehicles in China. *Energy for Sustainable Development*, *72*(1), 1–10. https://doi.org/10.1016/j.esd.2022.11.008

[3] Zhao, J., Liu, M., Zhang, B., Wang, X., Liu, D., Wang, J., & Zhu, Y. (2023). Review of lithium-ion battery fault features, diagnosis methods, and diagnosis procedures. *IEEE Internet of Things Journal*, *11*(11), 18936–18950. https://doi.org/10.1109/JIOT.2023.3324322

[4] Gu, X., Shang, Y., Kang, Y., Li, J., Mao, Z., & Zhang, C. (2023). An early minor-fault diagnosis method for lithium-ion battery packs based on unsupervised learning. *IEEE/CAA Journal of Automatica Sinica*, *10*(3), 810–812. https://doi.org/10.1109/JAS.2023.123099

[5] Huang, J. C., Shu, M. H., Lin, H. T., & Day, J. D. (2024). Transformer-based lithium battery fault diagnosis research for electric vehicles. *Journal of Intelligent & Fuzzy Systems*, *46*(4), 9329–9341. https://doi.org/10.3233/JIFS-237796

[6] Mao, Z., Gu, X., Li, J., Liu, K., Wang, T., & Shang, Y. (2023). An applicable minor short-circuit fault diagnosis method for automotive lithium-ion batteries based on extremum sample entropy. *IEEE Transactions on Power Electronics*, *39*(4), 4636–4644. https://doi.org/10.1109/TPEL.2023.3342412

[7] Liao, L., Yang, D., Li, X., Jiang, J., & Wu, T. (2024). Fault diagnosis of lithium-ion batteries based on wavelet packet decomposition and Manhattan average distance. *International Journal of Green Energy*, *21*(12), 2828–2842. https://doi.org/10.1080/15435075.2024.2332331

[8] Zhang, C., Li, S., Du, J., Zhang, L., Luo, W., & Jiang, Y. (2025). Graph-guided fault detection for multi-type lithium-ion batteries in realistic electric vehicles optimized by ensemble learning. *Journal of Energy Chemistry*, *106*(1), 507–522. https://doi.org/10.1016/j.jechem.2025.03.004

[9] Liu, T., Jin, Y. C., Wang, S., Zheng, Q., & Yang, G. (2023). Denoising method of weak fault acoustic emission signal under strong background noise of engine based on autoencoder and wavelet packet decomposition. *Structural Health Monitoring*, *22*(5), 3206–3224. https://doi.org/10.1177/14759217221143547

[10] Limouni, T., Yaagoubi, R., Bouziane, K., & Baali, E. H. (2023). Accurate one step and multistep forecasting of very short-term PV power using LSTM-TCN model. *Renewable Energy*, *205*(1), 1010–1024. https://doi.org/10.1016/j.renene.2023.01.118

[11] Li, S., Li, T., Sun, C., Chen, X., & Yan, R. (2023). WPConvNet: An interpretable wavelet packet kernel-constrained convolutional network for noise-robust fault diagnosis. *IEEE Transactions on Neural Networks and Learning Systems*, *35*(10), 14974–14988. https://doi.org/10.1109/TNNLS.2023.3282599

[12] Zhang, T., & Wang, Y. (2024). Fault diagnosis of wind turbine gearbox based on wavelet packet denoising and CNN-Swin Transformer-LSTM. In *Third International Conference on Image Processing, Object Detection, and Tracking (IPODT 2024)* (Vol. 13396, pp. 161–172). SPIE. https://doi.org/10.1117/12.3050446

[13] Hui, H., Guo, Y., Xu, C., Su, J., Huang, Q., & Yuzheng, L. (2025). Plunger motor fault analysis method based on improved wavelet packet threshold denoising and feature signal extraction. *Noise & Vibration Worldwide*, *56*(3), 186–202. https://doi.org/10.1177/09574565251319276

[14] Qin, S., Tao, J., & Zhao, Z. (2023). Fault diagnosis of wind turbine pitch system based on LSTM with multi-channel attention mechanism. *Energy Reports*, *10*(1), 4087–4096. https://doi.org/10.1016/j.egyr.2023.10.076

[15] Ren, C., Li, H., Lei, J., Liu, J., Li, W., Gao, K., & Yu, T. (2023). A CNN-LSTM–based model to fault diagnosis for CPR1000. *Nuclear Technology*, *209*(9), 1365–1372. https://doi.org/10.1080/00295450.2023.2199098

[16] Feng, R., Zhang, X., Liu, X., Cong, Y., Li, X., Yang, D., & Xu, J. (2024). Research on capacity configuration scheme of hybrid energy storage equipment in wind farm based on wavelet packet decomposition. In *20th International Conference on AC and DC Power Transmission 2024 (ACDC 2024)* (pp.1207–1213). IET. https://doi.org/10.1049/icp.2024.2451

[17] Jia, Y., Zhang, L., & Wang, H. (2024). Research on fault diagnosis of lithium-ion battery based on wavelet packet energy entropy and SVM. In 2024 4th International Conference on Electrical Engineering and Automation (ICEEA 2024). Atlantis. Press. https://doi.org/10.1080/15435075.2024.2332331

[18] Lu, Y., Zhang, M., Chen, Y., Ju, J., Chen, F., Bai, K., & Wang, X. (2025). A newly developed multi-strategy optimization algorithm framework based on the adaptive switching approach coupled with grey wolf optimizer. *Knowledge and Information Systems*, *67*(7), 5571–5617. https://doi.org/10.1007/s10115-025-02360-2

[19] Lawah, A. I., Ibrahim, A. A., Salih, S. Q., Alhadawi, H. S., & JosephNg, P. S. (2023). Grey wolf optimizer and discrete chaotic map for substitution boxes design and optimization. *IEEE Access*, *11*(1), 42416–42430. https://doi.org/10.1109/ACCESS.2023.3266290

[20] Ma, C., Gu, K., Zhao, Y., & Wang, T. (2025). Research on highway traffic flow prediction based on a hybrid model of ARIMA–GWO–LSTM. *Neural Computing and Applications*, *37*(20), 14703–14722. https://doi.org/10.1007/s00521-024-10550-2

[21] Pang, J., Luo, W., Yao, Z., Chen, J., Dong, C., & Lin, K. (2024). Water quality prediction in urban waterways based on wavelet packet denoising and LSTM. *Water Resources Management*, *38*(7), 2399–2420. https://doi.org/10.1007/s11269-024-03774-3